Star Formation News Letter No. 366, #16-29：工藤哲洋

16. **PENELLOPE IV. A comparison between optical forbidden lines and H_2 UV lines in the Orion OB1b and σ-Ori associations**
M. Gangi, B. Nisini, C. F. Manara, K. France, S. Antoniucci, K. Biazzo, T. Giannini, G. J. Herczeg, J. M. Alcalá, A. Frasca, K. Maucó, J. Campbell-White, M. Siwak, L. Venuti, P. C. Schneider, Á. Kóspál, A. Caratti o Garatti, E. Fiorellino, E. Rigliaco, R. K. Yadav ★ Observing the spatial distribution and excitation processes of

17. **Post-outburst evolution of bonafide FUor V2493 Cyg: A Spectro-photometric monitoring**
Arpan Ghosh, Saurabh Sharma, Joe P. Ninan, Devendra K. Ojha, Bhuwan C. Bhatt, D. K. Sahu, Tapas Baug, R. K. Yadav, Puji Irawati, A. S. Gour, Neelam Panwar, Rakesh Pandey, Tirthendu Sinha, Aayushi Verma

18. **Turbulence in compact to giant H II regions**
J. García-Vázquez, William J. Henney, H. O. Castañeda ★ Radial velocity fluctuations on the plane of the sky are a

19. **Similar levels of deuteration in the pre-stellar core L1544 and the protostellar core HH211**
K. Giers, S. Spezzano, P. Caselli, E. Wirström, O. Sipilä, J. E. Pineda, E. Redaelli, C. T. Bop, F. Lique ★ In

2 20. **JWST Peers into the Class I Protostar TMC1A: Atomic Jet and Spatially Resolved Dissociative Shock Region**
Daniel Harsono, Per Bjerkeli, Jon Ramsey, Klaus Pontoppidan, Lars Kristensen, Jes Jørgensen, Hannah Calcutt, Zhi-Yun Li, Adele Plunkett ★ Outflows and winds launched from young stars play a crucial role in the evolution

1 21. **Inner Planetary System Gap Complexity is a Predictor of Outer Giant Planets**
Matthias Y. He, Lauren M. Weiss ★ The connection between inner small planets and outer giant planets is crucial to our

22. **A Constraint on the Amount of Hydrogen from the CO Chemistry in Debris Disks**
Kazunari Iwasaki, Hiroshi Kobayashi, Aya E. Higuchi, Yuri Aikawa ★ The faint CO gases in debris disks are easily

23. **Investigating the Impact of Metallicity on Star Formation in the Outer Galaxy. I. VLT/KMOS Survey of Young Stellar Objects in Canis Major**
Dominika Itrich, Agata Karska, Marta Sewiło, Lars E. Kristensen, Gregory J. Herczeg, Suzanne Ramsay, William J. Fischer, Benoît Tabone, Will R. M. Rocha, Maciej Koprowski, Ngân Lê, Beata Deka-Szymankiewicz

24. **Investigating the Impact of Metallicity on Star Formation in the Outer Galaxy. I. VLT/KMOS Survey of Young Stellar Objects in Canis Major**
Dominika Itrich, Agata Karska, Marta Sewiło, Lars E. Kristensen, Gregory J. Herczeg, Suzanne Ramsay, William J. Fischer, Benoît Tabone, Will R. M. Rocha, Maciej Koprowski, Ngân Lê, Beata Deka-Szymankiewicz

4 25. **In search for infalling clumps in molecular clouds – A catalogue of CO blue-profiles**
Zhibo Jiang, Shaobo Zhang, Zhiwei Chen, Yang Yang, Shuling Yu, Haoran Feng, Ji Yang, the MWISP group ★

26. **Near infrared view on the photodissociation regions S255, S257, NGC7538 and S140**
M. S. Kirsanova, A. M. Tatarnikov, P. A. Boley, D. S. Wiebe, N. A. Maslennikova, A. A. Tatarnikov ★ We

27. **Classification of Chandra X-ray Sources in Cygnus OB2**
Vinay L. Kashyap, Mario G. Guarcello, Nicholas J. Wright, Jeremy J. Drake, Ettore Flaccomio, Tom L. Aldcroft, Juan F. Albacete Colombo, Kevin Briggs, Francesco Damiani, Janet E. Drew, Eduardo L. Martin, Giusi Micela, Tim Naylor, Salvatore Sciortino ★ We have devised a predominantly Naive Bayes method to classify

28. **SPYGLASS. IV. New Stellar Survey of Recent Star Formation within 1 kpc**
Ronan Kerr, Adam Kraus, Aaron Rizzuto ★ Young stellar populations provide a powerful record that traces millions

3 29. **The magnetic fields around the cometary globules, L328, L323 and L331**
Siddharth Kumar, Archana Soam, Nirupam Roy ★ This work presents the magnetic field geometry in a complex of

21. **Inner Planetary System Gap Complexity is a Predictor of Outer Giant Planets**

Matthias Y. He, Lauren M. Weiss ★

The connection between inner small planets and outer giant planets is crucial to our understanding of planet formation across a wide range of orbital separations. While Kepler provided a plethora of compact multi-planet systems at short separations ($\lesssim$ 1 AU), relatively little is known about the occurrence of giant companions at larger separations and how they impact the architectures of the inner systems. Here, we use the catalog of systems from the Kepler Giant Planet Search (KGPS) to study how the architectures of the inner transiting planets correlate with the presence of outer giant planets. We find that for systems with at least three small transiting planets, the distribution of inner-system gap complexity ($\mathcal{C}$), a measure of the deviation from uniform spacings, appears to differ ($p \lesssim 0.02$) between those with an outer giant planet ($50M_\oplus \leq M_p \sin i \leq 13M_{\rm Jup}$) and those without any outer giants. All four inner systems (with 3+ transiting planets) with outer giant(s) have a higher gap complexity ($\mathcal{C} > 0.32$) than 79% (19/24) of the inner systems without any outer giants (median $\mathcal{C} \simeq 0.06$). This suggests that one can predict the occurrence of outer giant companions by selecting multi-transiting systems with highly irregular spacings. We do not find any correlation between outer giant occurrence and the size (similarity or ordering) patterns of the inner planets. The larger gap complexities of inner systems with an outer giant hints that massive external planets play an important role in the formation and/or disruption of the inner systems.

- 内側の小さな惑星(SP)が外側の大きな惑星(OG)からどのような影響を受けているのかを，観測結果から推定しようとした論文。
- Kepler Giant Planet Search (KGPS) の観測結果を用いている。KGPSは，ケプラーで発見された内側の小さな惑星について，外側にある大きな惑星をドップラー法で探査しているプロジェクト。
- OGがある惑星系では，公転軌道の間隔が等間隔からずれている傾向がある。
- SPの質量配分については，OGの影響は特に見られなかった。

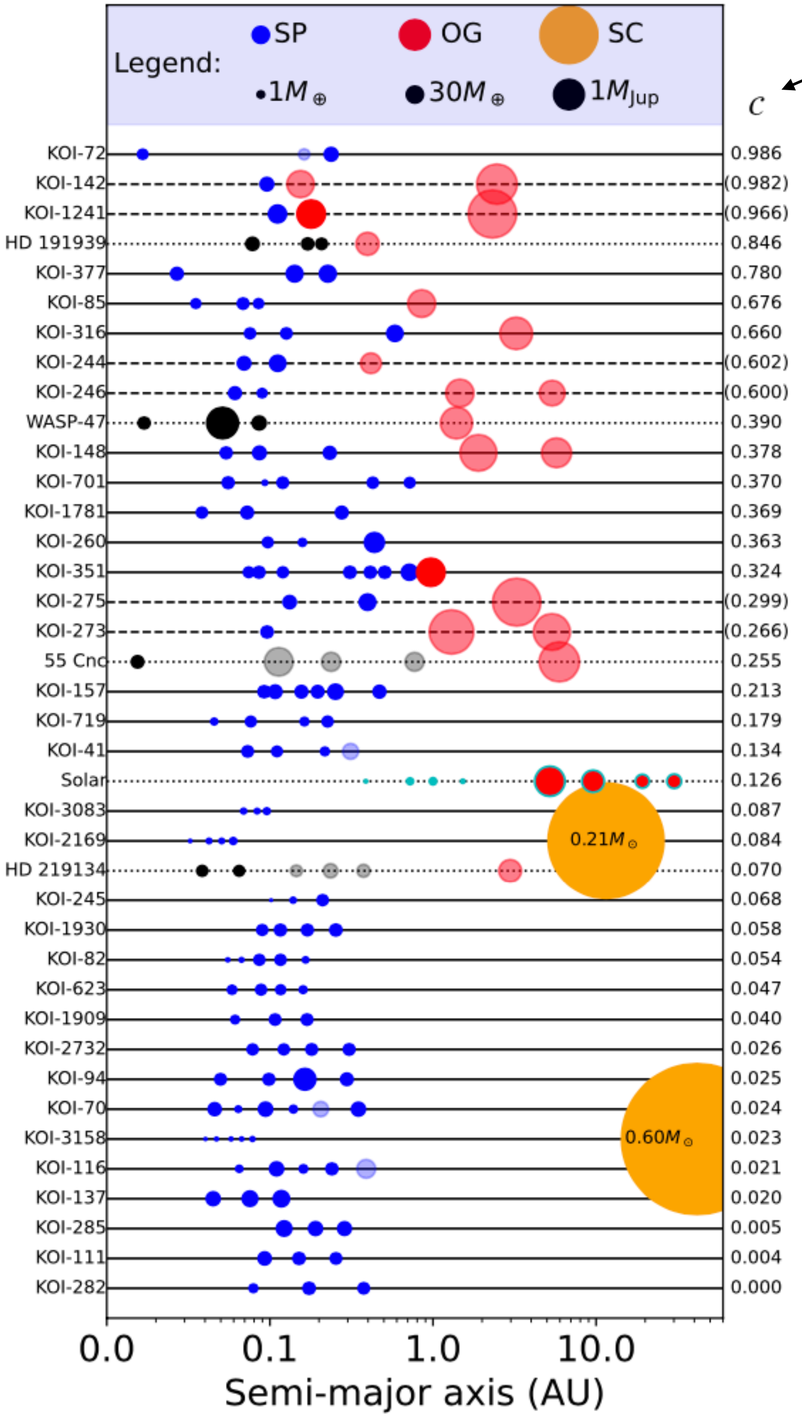

Gap complexity（0以上1以下）
軌道間隔が等間隔からずれていることを示す指標。値が大きいほど，等間隔からずれている。

SP：Small Planets 地球質量の50倍以下

OG：Outer Giants 地球質量の50倍以上，木星質量の13倍以下

SC：Stellar Companions 恒星

OGがある惑星は Gap complexity が大きい傾向にある。

Figure 1. Architectures gallery of the KGPS and other systems with at least three planets. Each row corresponds to one planetary system (as labeled on the left y-axis) and is plotted along the semi-major axis (x-axis, log scale). The point sizes are proportional to the square root of the planet masses ($M_p \sin i$ or masses from a mass-radius relation). The point colors denote small planets (SP; blue), outer giants (OG; red), and stellar companions (SC; orange), as also labeled in the legend. Black points indicate inner planets in systems that are not part of the KGPS sample (also denoted by dotted lines). Faded points indicate non-transiting planets. The systems are sorted by the gap complexity ($\mathcal{C}$) of the *inner system* (where there are at least three planets excluding any OGs or SCs), as labeled on the right y-axis, or $\mathcal{C}$ of the whole system when there are fewer than 3 SPs (in parentheses; these systems are also denoted by the dashed lines). For reference, the solar system is also plotted (cyan points) with the same convention, where the planets from Jupiter and beyond are categorized as OGs and excluded from the calculation of $\mathcal{C}$.

Gap complexity に対する累積相対度数分布

Keplerで発見された全分布と
今回の全分布の比較

OGがあるものと無いものとの比較

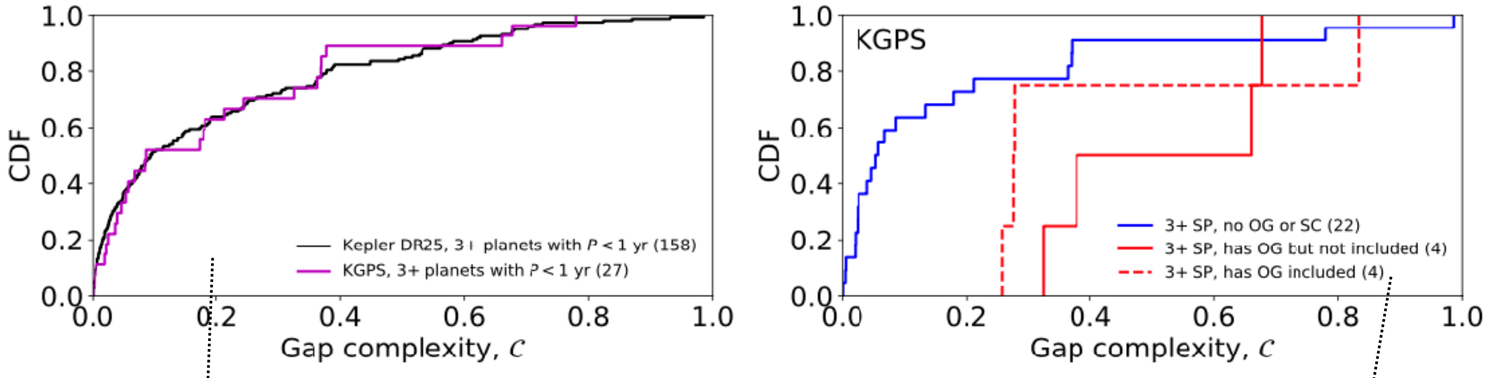

Figure 2. Cumulative distributions of gap complexity ($\mathcal{C}$). **Left:** distributions for all systems with at least three planets within 1 yr in the *Kepler* DR25 catalog (black) and in the KGPS sample (magenta). While there are fewer such systems in the KGPS sample (as indicated by the numbers in parentheses), the distribution of $\mathcal{C}$ is consistent with being drawn from the same distribution as the *Kepler* DR25 systems. **Right:** distributions for subsets of the KGPS sample (all with at least three inner small planets); the blue line includes systems with no outer giants, while the red lines include only the systems with at least three small planets *and* at least one outer giant planet, where the outer giant(s) are either excluded from (solid) or included in (dashed) the calculation of $\mathcal{C}$.

2つの分布がほぼ同じなので，今回選んだ
サンプルにバイアスは無いだろう。

赤と青の分布がだいぶ異なるので，
OGの影響はあるだろう。

質量配分を示すパラメータ（3種類）に対する累積相対度数分布

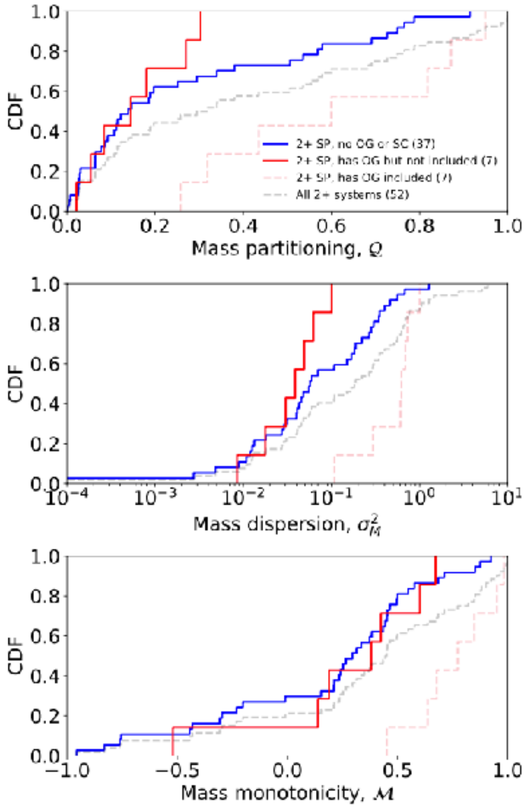

Figure 4. Cumulative distributions of planet mass partitioning ($\mathcal{Q}$; **top**), mass dispersion (σ_M^2; **middle**), and mass monotonicity ($\mathcal{M}$; **bottom**), for various subsets of the KGPS sample (systems with at least two planets). In each panel, the solid lines include the *inner small planets* for systems with no outer giant planets (blue) and for systems with outer giant planet(s) (red). We also show the distribution for the latter sample including the outer giant planets in the calculation (dashed red line), which by definition typically increase all three metrics. For reference, all KGPS systems with at least two planets are denoted by the dashed gray line; there are more systems in this sample than the sum of the samples in the blue and red lines because some systems have exactly one transiting planet and one outer giant planet.

Mass partitioning: Q　　Mass dispersion: σ_M^2　　Mass monotonicity:$\mathcal{M}$

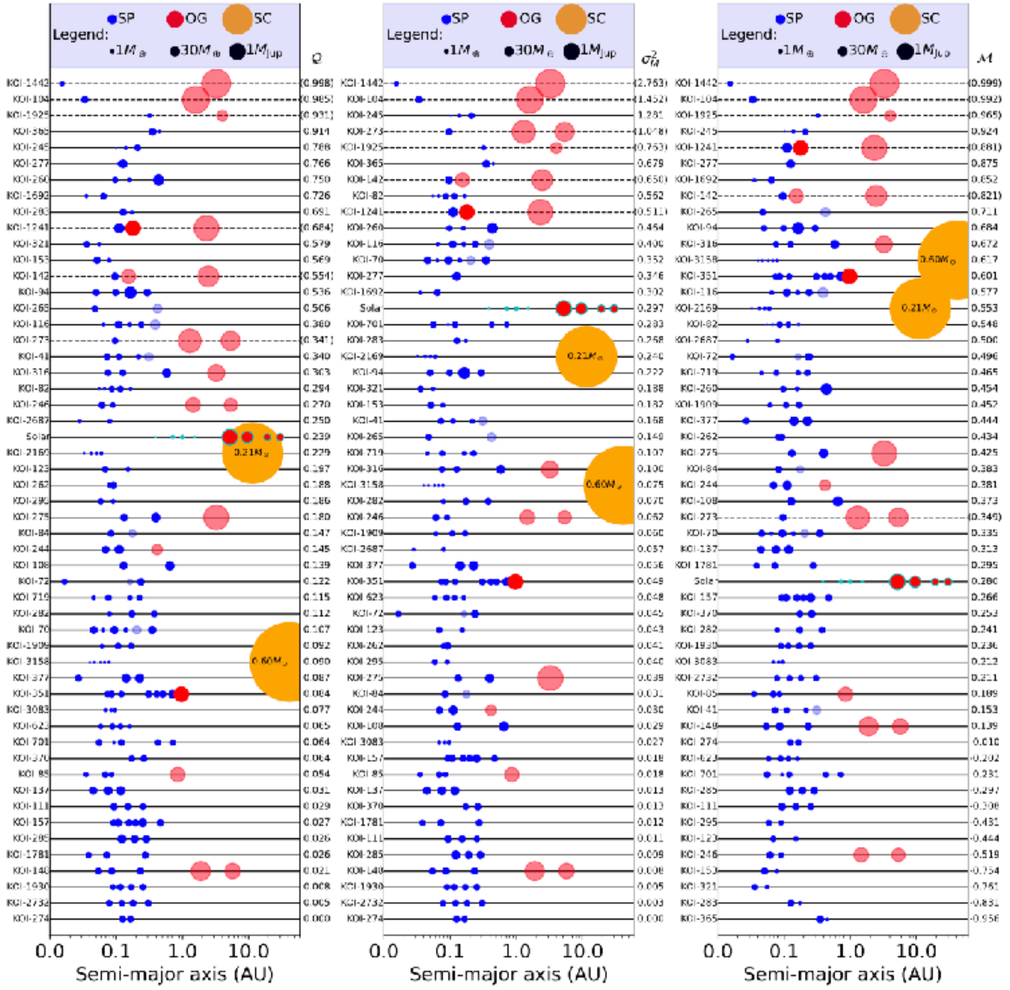

Figure 5. Architectures gallery of the KGPS systems with at least two planets. The axes, legend, and conventions are identical to those in Figure 1. **Left:** The systems sorted by the mass partitioning ($\mathcal{Q}$) of the *inner system* (i.e. SPs only, where there are at least two), as labeled on the right y-axis, or the mass partitioning of the whole system when there are fewer than 2 SPs (denoted by the numbers in parentheses; these systems are also denoted by the dashed lines). **Middle:** The same systems, sorted and labeled by mass dispersion (σ_M^2). **Right:** The same systems, sorted and labeled by mass monotonicity ($\mathcal{M}$). As in Figure 1, the solar system is also plotted (cyan points) with the same convention, where the planets from Jupiter and beyond are excluded from the calculation of $\mathcal{Q}$ or σ_M^2 or $\mathcal{M}$. For all three metrics, there is no apparent correlation between the inner system and the occurrence of outer giant planets.

質量配分については，OGのあるなしには関係が見られない。

20. **JWST Peers into the Class I Protostar TMC1A: Atomic Jet and Spatially Resolved Dissociative Shock Region**

Daniel Harsono, Per Bjerkeli, Jon Ramsey, Klaus Pontoppidan, Lars Kristensen, Jes Jørgensen, Hannah Calcutt, Zhi-Yun Li, Adele Plunkett ★

Outflows and winds launched from young stars play a crucial role in the evolution of protostars and the early stages of planet formation. However, the specific details of the mechanism behind these phenomena, including how they affect the protoplanetary disk structure, are still debated. We present *JWST* NIRSpec Integral Field Unit (IFU) observations of atomic and H_2 lines from $1 - 5.1$ μm toward the low-mass protostar TMC1A. For the first time, a collimated atomic jet is detected from TMC1A in the [Fe II] line at 1.644 μm along with corresponding extended H_2 2.12 μm emission. Towards the protostar, we detected spectrally broad H I and He I emissions with velocities up to 300 km/s that can be explained by a combination of protostellar accretion and a wide-angle wind. The 2μm continuum dust emission, H I, He I, and O I all show emission from the illuminated outflow cavity wall and scattered line emission. These observations demonstrate the potential of *JWST* to characterize and reveal new information about the hot inner regions of nearby protostars. In this case, a previously undetected atomic wind and ionized jet in a well-known outflow.

- JWSTで，原始星（Class I：TMC1A）にジェットを発見したという論文。
- [FeII]（1.644μm）とH_2（2.12μm）の輝線で，100 au スケール程度のコリメートした空間構造が得られた。
- 加えて，水素原子のパッシェン系列などから，ジェットを示唆する輝線の速度構造が得られた。

Class I protostar TMC1A のこれまでの観測

- 質量　～0.45 $M_\odot$
- 距離　140 pc （おうし座分子雲の中）
- 大スケールの双極分子流　～6000 au
- 円盤風が^{12}CO(J=2-1)で観測されている(ALMA)
- 最も早いガスの運動が^{12}CO(4.6μm)で　～ 75km/s と観測されている。
- ジェットは，SiOやH_2Oのラインでは観測されていない。

⟶ 今回それが[FeII]などで観測された。

JWSTのNIRSpecという装置で得たスペクトルの全体像

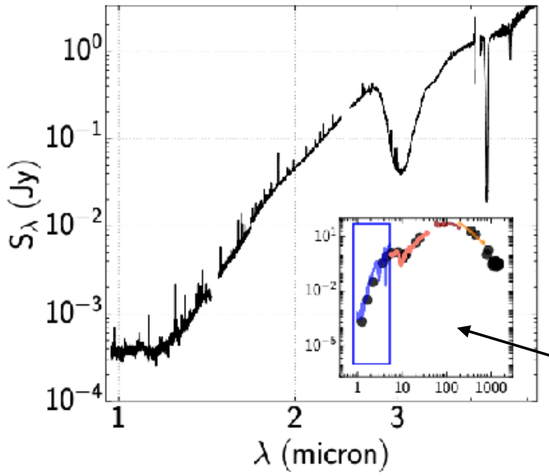

他の観測で得られていた
スペクトルとの合体

Figure 1. NIRSpec spectrum extracted from the central 0.″3 spaxels. The spectral energy distribution of TMC1A from other observations is shown in the inset along with the NIRSpec data in blue. The Photometric data points (black) are from Kristensen et al. (2012) (includes points from Skrutskie et al. 2006, Di Francesco et al. 2008, Evans et al. 2009, Karska et al. 2013, and Green et al. 2013) . *Herschel* PACS observations of Green et al. (2013) are shown in orange. The *SPITZER* IRS spectrum (pink; Lahuis et al. 2010) is overlaid.

輝線を見るために規格化したスペクトル

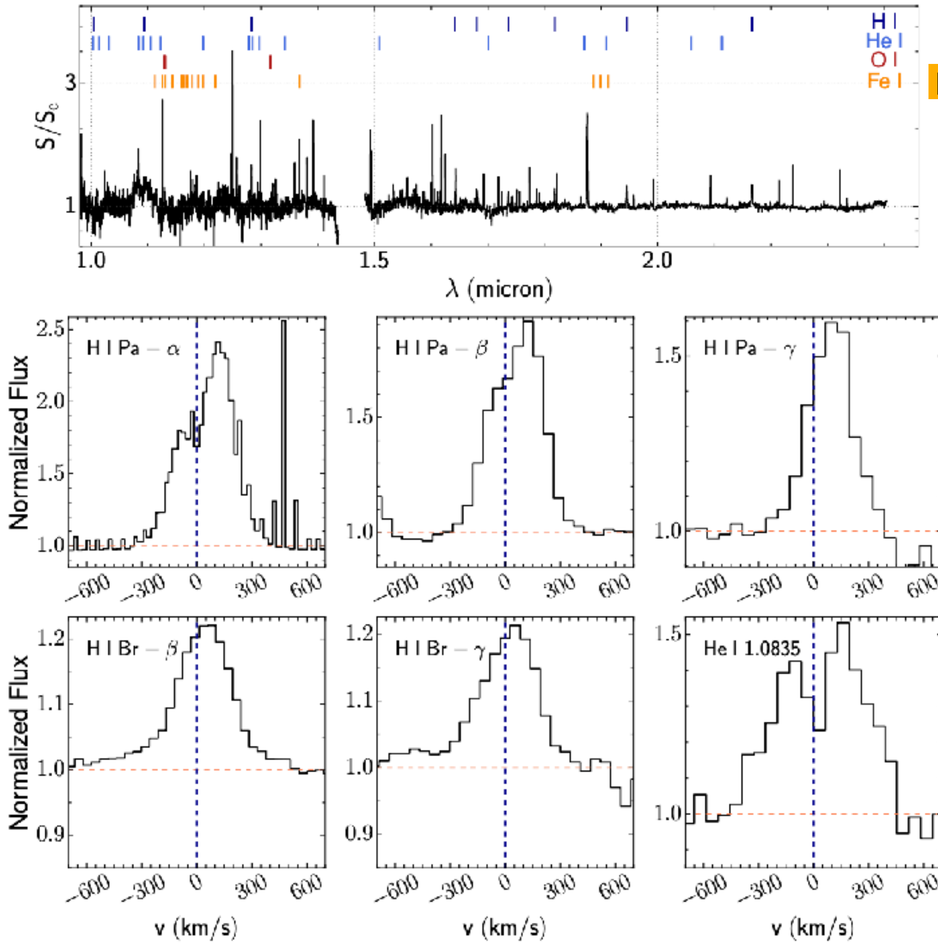

Figure 2. *Top:* Normalized spectrum of TMC1A. The spectrum has been normalized with a global continuum fit constructed with a polynomial of degrees 5 to 7. Transitions of H I, He I, O I, and Fe II with high A_{ij} values are indicated by the vertical colored lines above the spectrum. *Bottom:* Zoom-in spectra of the brightest H I lines and the He I λ1.0835 line. The spectral resolution is $\Delta v \sim 100 - 150$ km/s.

円盤風と降着流の両方を見ているのではないか

各スペクトル強度の2次元マップ

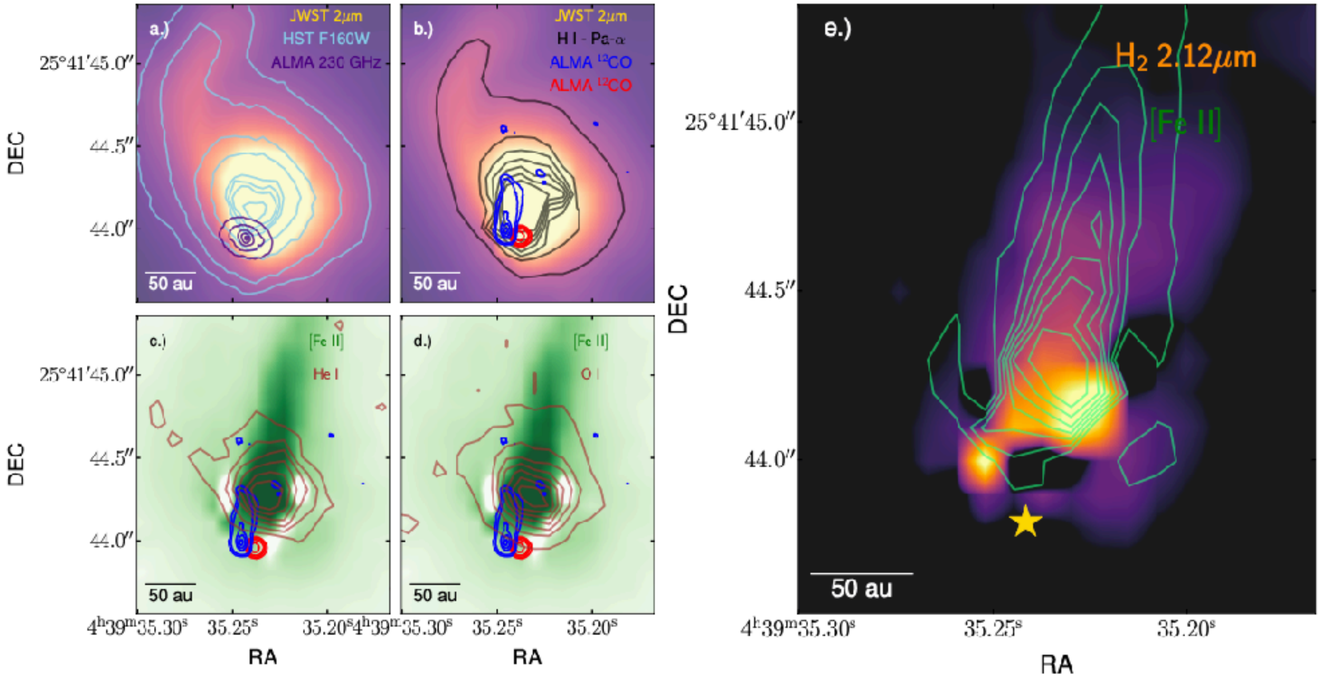

Figure 3. *a.) JWST* 2μm continuum map is shown in color. A linear scale between 0.5% to 99% of the intensity distribution is used. We have overlaid the *HST* F160W and ALMA 230 GHz continuum maps on top of the 2μm map to orient our results with respect to previous observations. The contours are chosen to highlight the features of the *HST* image and the location of the millimeter dust disk. *b.)* The integrated H I Pa-α map is shown by the black contour lines over top of the 2μm map. Contours from 95% to 98% of the intensity distribution are used. ALMA observations of the blue- and red-shifted rotational transition of ^{12}CO ($J = 2-1$) are shown by the blue and red contours, respectively. The ^{12}CO $J = 2-1$ line is only showing velocities > 1.5 km/s from systemic. The contours are chosen to highlight the orientation of the ^{12}CO $J = 2-1$ gas. *c.)* A comparison between [Fe II] 1.644 μm, He I λ10835, and ^{12}CO $J = 2-1$ line emission. The integrated [Fe II] line is shown in the background in green with a linear scale spanning between 60% to 99% of the intensity distribution. The He I map is shown by the brown contours with levels from 95% to 97% of the intensity distribution). *d.)* A comparison between [Fe II] 1.644 μm, O I λ1.12, and ^{12}CO $J = 2-1$ lines. The contours of O I (in brown) are also showing the brightest components (95%–97% of the intensity distribution). *e.)* The integrated [Fe II] map is overlaid on top of the integrated H_2 2.12μm map. The H_2 map is drawn with colors spanning from 5σ up to the peak intensity. The green contours show [Fe II] but only the brightest pixels in the map (> 96% of the intensity distribution). The center of the millimeter dust disk is indicated by the star. In each panel, a 50 au scale bar is show in the bottom left.

観測結果から想像される描像

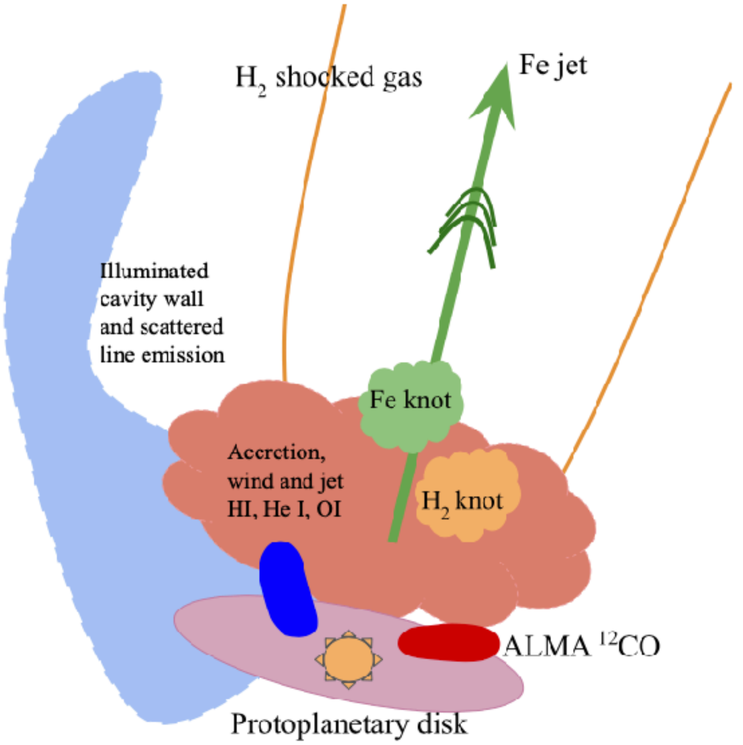

Figure 4. Cartoon of TMC1A's physical structure. The three major components that are traced by the hot gas lines are accretion to the protostar, the jet, and the illuminated cavity wall. The disk and the cold wind as traced with ALMA are also indicated.

29. **The magnetic fields around the cometary globules, L328, L323 and L331**

Siddharth Kumar, Archana Soam, Nirupam Roy ★ This work presents the magnetic field geometry in a complex of three cometary (with head-tail morphology) globules, namely LDN 323, LDN 328, and LDN 331, using R-band polarization measurements of background stars. These observations were combined with a Planck sky survey to study the large-scale morphology of the magnetic fields in the region. The distances of the target stars were adopted from the Gaia catalog. The variation of degree of polarization and polarization position angle with distances of stars is analyzed. The field geometry is mostly found to follow the cometary shape of the cloud, with some randomness at certain locations. For studying the correlation between cloud morphology and magnetic field orientations, a modified version of the Histogram of Relative Orientation analysis was employed.

- Cometary globule のL328, L323, L331 の磁場の構造を，背景星から得られるRバンドの偏光観測から得たという論文。
- 磁場は，おおよそ，分子雲の彗星状の細長い形の方向に沿っている。
- （磁場の強さの情報がない？）

Cometary globule L328, L323, L331

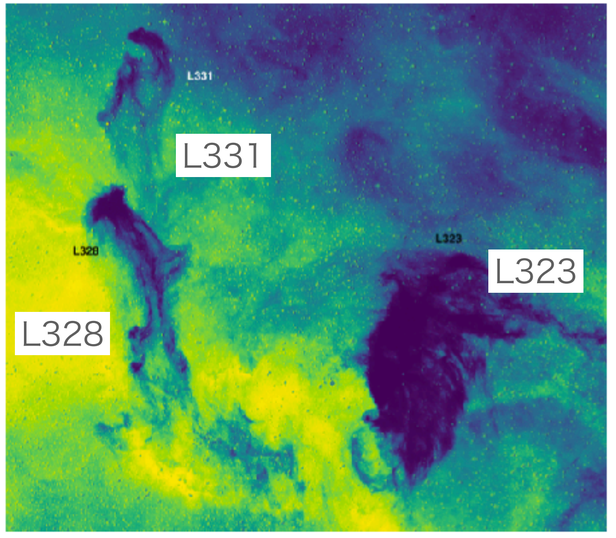

距離 ～ 220 pc
大きさ ～ 15′（～ 1 pc）

Figure 1. The figure above shows the Hα image of the region, showing all three clouds L323, L328 and L331.

偏光度と星の距離

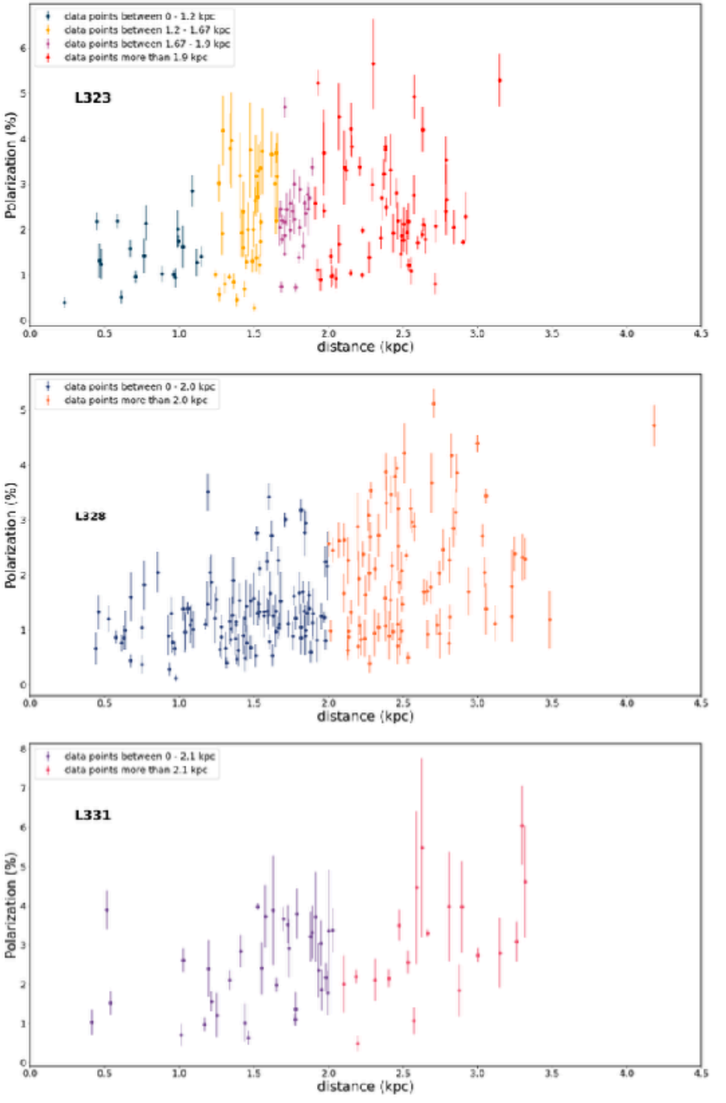

Figure 4. The figure above shows the polarization percentage as a function of distance obtained from Bailer-Jones 2021 for the clouds (from top to bottom) L323, L328, and L331

比較のため：Plankの赤外線から得た偏光

今回の観測で得た偏光

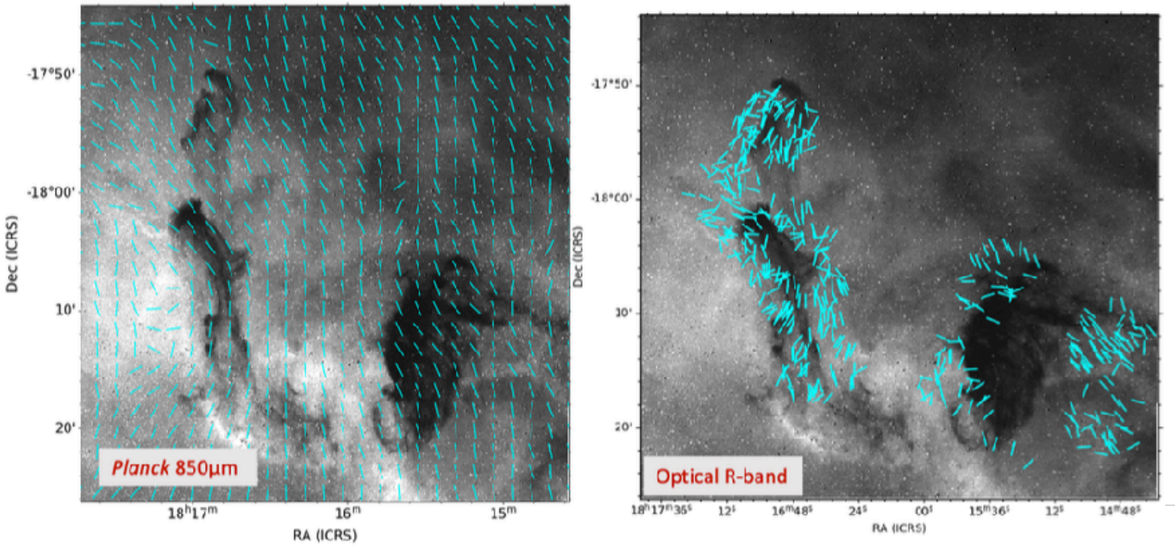

Figure 3. The figure above shows the plane of the sky magnetic field inferred from *Planck* polarization vectors on the left and optical polarization vectors on the right, both plotted on an R-band subtracted Hα image.

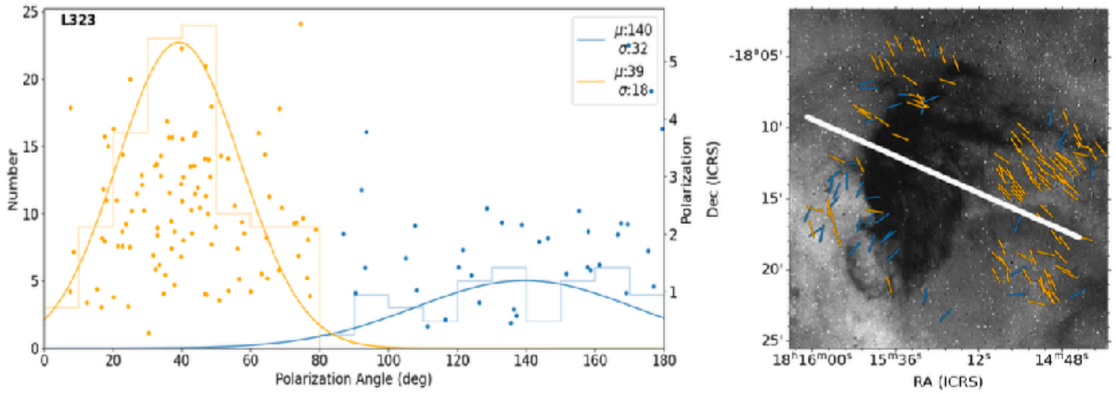

Figure 6. The figure above shows the distribution of polarization angles for L323 with a Gaussian fit to the polarization angle distribution on the left. The distribution has been divided into smaller distributions **I** and **II** colored as yellow and blue respectively. The colored dots represent the polarization of stars, where larger dots show higher polarization and vice-versa. On the right we have distributions **I** and **II** plotted on the cloud with the major axis of the cloud plotted in white.

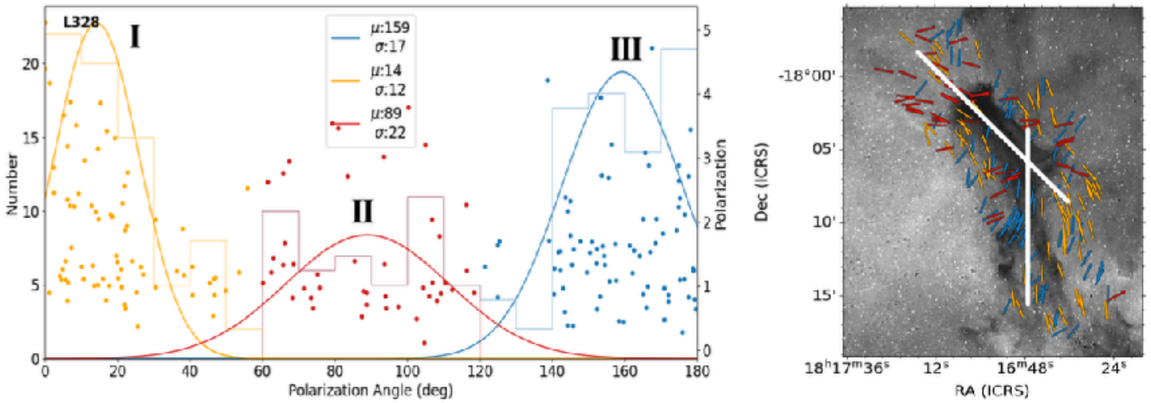

Figure 7. The figure above shows the distribution of polarization angles for L328 with a Gaussian fit to the polarization angle distribution on the left. The distribution has been divided into smaller distributions **I, II** and **III** colored as yellow, red and blue respectively. The colored dots represent the polarization of stars, where larger dots show higher polarization and vice-versa. On the right we have distributions **I, II** and **III** plotted on the cloud. The major axis for the head and tail has been plotted in white.

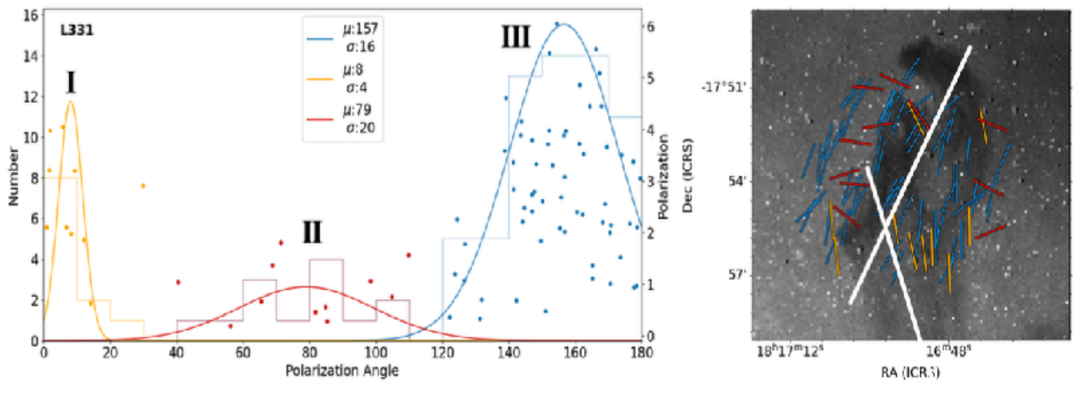

Figure 8. The figure above shows the distribution of polarization angles for L331 with a Gaussian fit to the polarization angle distribution on the left. The distribution has been divided into smaller distributions **I, II** and **III** colored as yellow, red and blue respectively. The colored dots represent the polarization of stars, where larger dots show higher polarization and vice-versa. On the right we have distributions **I, II** and **III** plotted on the cloud. The major axis for the head and tail has been plotted in white.

細かいランダムな構造もあるが，おおむね分子雲の細長い構造に沿っている。

25. **In search for infalling clumps in molecular clouds – A catalogue of CO blue-profiles**

Zhibo Jiang, Shaobo Zhang, Zhiwei Chen, Yang Yang, Shuling Yu, Haoran Feng, Ji Yang, the MWISP group ★

We have started a systematic survey of molecular clumps with infall motions to study the very early phase of star formation. Our first step is to utilize the data products by MWISP to make an unbiased survey for blue asymmetric line profiles of CO isotopical molecules. Within a total area of ∼ 2400 square degrees nearby the Galactic plane, we have found 3533 candidates showing blue-profiles, in which 3329 are selected from the ^{12}CO&^{13}CO pair and 204 are from the ^{13}CO&C^{18}O pair. Exploration of the parametric spaces suggests our samples are in the cold phase with relatively high column densities ready for star formation. Analysis of the spatial distribution of our samples suggests that they exist virtually in all major components of the Galaxy. The vertical distribution suggest that the sources are located mainly in the thick disk of ∼ 85 parsec, but still a small part are located far beyond Galactic midplane. Our follow-up observation indicates that these candidates are a good sample to start a search for infall motions, and to study the condition of very early phase of star formation.

- 星形成初期の落下運動（infall motion）を示す分子雲の無バイアスサーベイ観測の論文。
- 2400 square degree の領域に，3533個の落下運動を示す分子雲を観測。
- それらの分子雲の多くは銀河系の渦状腕上に分布し，縦方向には〜85 pc の厚みの thick disk の中に多く存在していた。

^{12}COが光学的に厚く^{13}COが光学的に薄い（Pair-1）

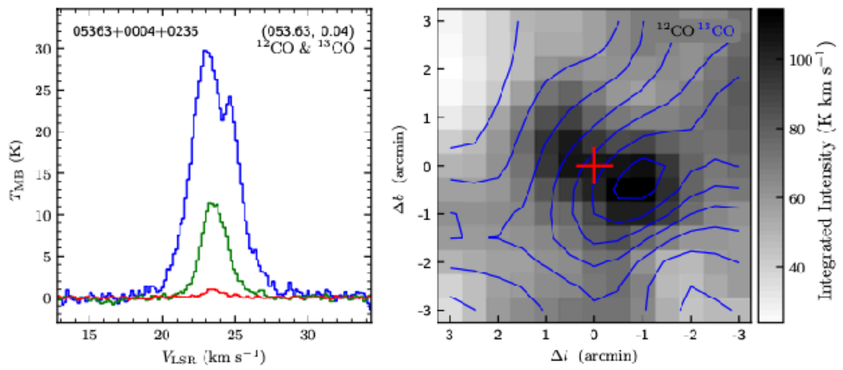

(a) 05363+0004+0235

^{13}COが光学的に厚く$C^{18}O$が光学的に薄く（Pair-2）

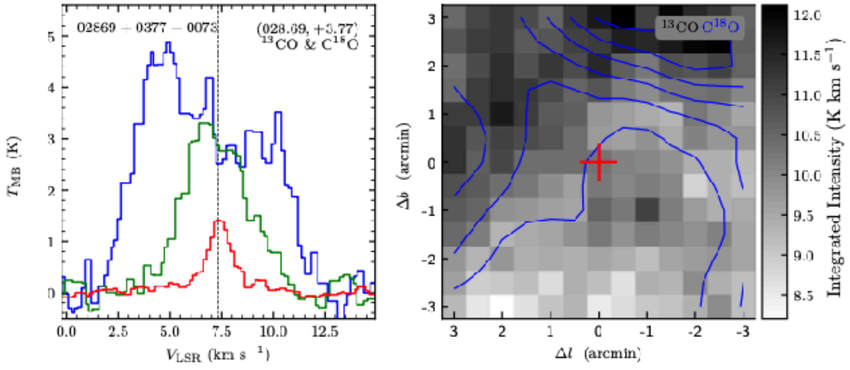

(b) 02869+0377+0073

赤：$C^{18}O$，　緑：^{13}CO，　青：^{12}CO

Fig. 2: The spectra (left) and gas distributions (right) of the candidates. On the left panels, the red, green and blue lines represent $C^{18}O$, ^{13}CO and ^{12}CO emissions, respectively. To enhance s/n ratios of the lines, the spectra are smoothed with median filter for each 3 velocity channels. For the same reason, the $C^{18}O$ spectra are also smoothed with 3×3 spatial pixels, The dashed line indicates the system velocity. On the upper-right corners we indicate the Galactic coordinates (l, b), and the line-pairs used in the searching procedure. On the upper-left are the name codes of the candidates. The right panels show the integrated intensity map of the optically thin lines (contours) overlaid on those of the optically thick lines (grey scale). The red pluses indicate the positions where the blue-profiles are detected.

Pair-1（^{12}CO-^{13}COのPair）が3329個,
Pair-2（^{13}CO-$C^{18}O$のPair）が204個

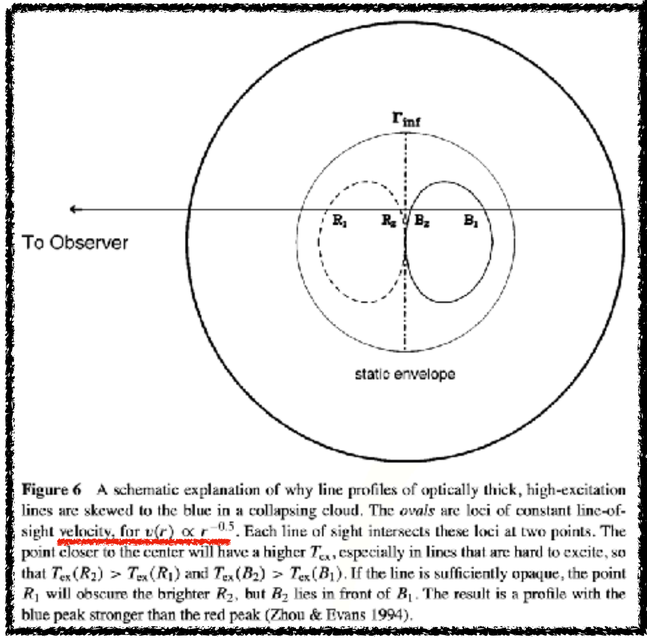

Figure 6 A schematic explanation of why line profiles of optically thick, high-excitation lines are skewed to the blue in a collapsing cloud. The *ovals* are loci of constant line-of-sight velocity, for $v(r) \propto r^{-0.5}$. Each line of sight intersects these loci at two points. The point closer to the center will have a higher T_{ex}, especially in lines that are hard to excite, so that $T_{ex}(R_2) > T_{ex}(R_1)$ and $T_{ex}(B_2) > T_{ex}(B_1)$. If the line is sufficiently opaque, the point R_1 will obscure the brighter R_2, but B_2 lies in front of B_1. The result is a profile with the blue peak stronger than the red peak (Zhou & Evans 1994).

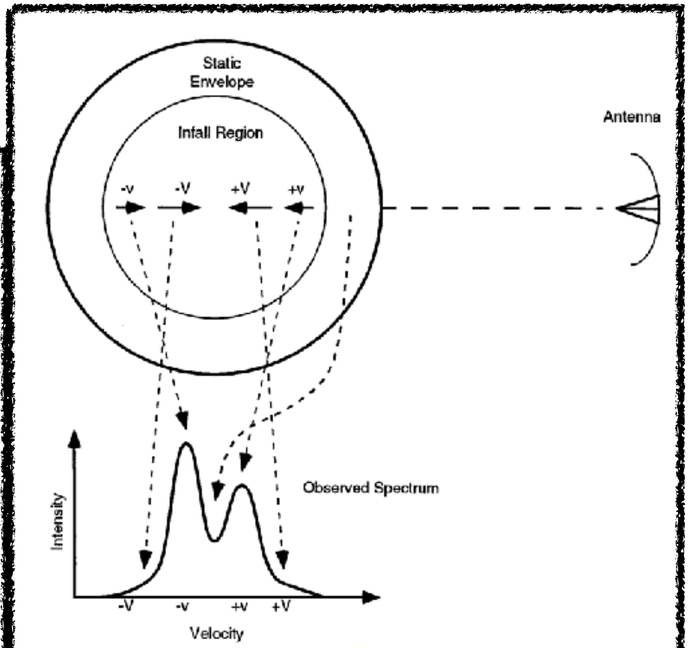

Figure 5 The origin of various parts of the line profile for a cloud undergoing inside-out collapse. The static envelope outside r_{inf} produces the central self-absorption dip, the blue peak comes from the back of the cloud, and the red peak from the front of the cloud. The faster collapse near the center produces line wings, but these are usually confused by outflow wings.

(Evans, Neal J., I. 1999, ARA&A, 37, 311)

Pair-1 （^{12}CO-^{13}COのPair）

Pair-2 （^{13}CO-C^{18}OのPair）

相対度数分布

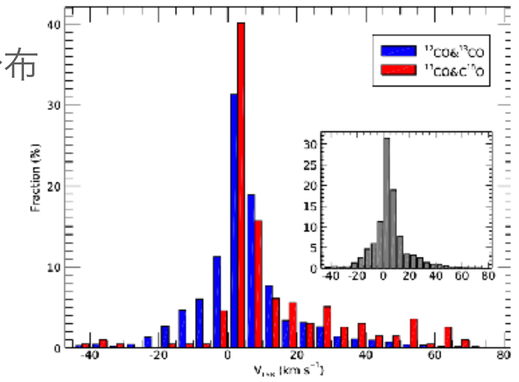

(a) Vc

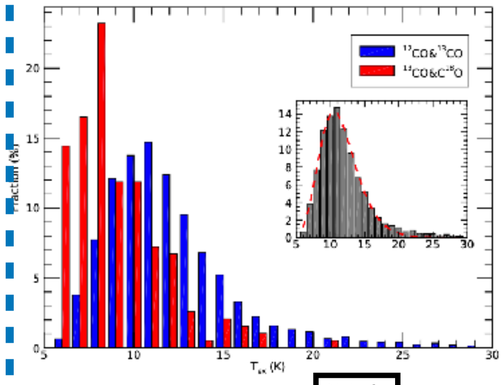

(b) T_{ex}

温度

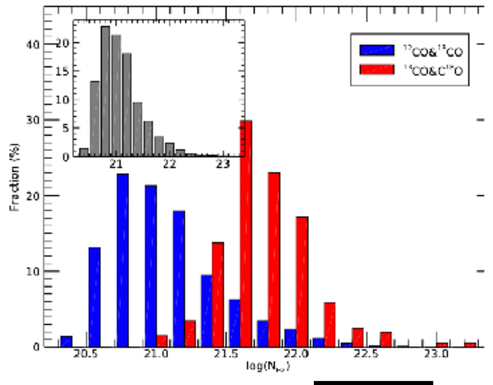

(c) N(H_2)

柱密度

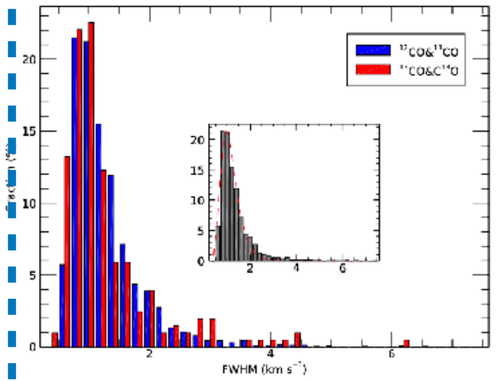

(d) FWHM

Fig. 4: Frequency distributions of (a) central velocities; (b) excitation temperatures; (c) derived H_2 column densities (cm^{-2} on log scale); (d) Line widths (FWHM) of the optically thin lines. In the inset of (b), the dashed curve is a log-normal fit with $(\sigma, \mu) = (2.41, 0.25)$ to overall T_{ex} distribution. In the inset of (d), the dashed curve is the best log-normal fit with $(\sigma, \mu) = (0.34, 0.076)$, to the overall distribution of FWHMs. For each parameter, the bins for both Pair-1 and Pair-2 as well as for the overall are set to same.

空間分布

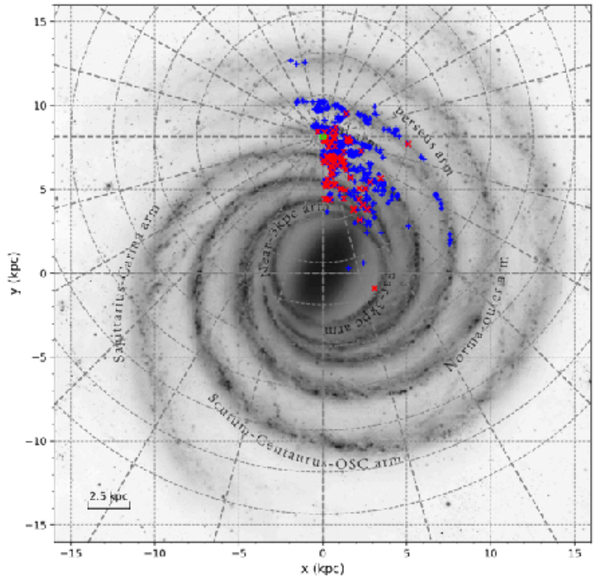

Fig. 7: Spatial distribution of the infall candidates overlaid on the imaginary face-on view of the Milky Way (credit: Xing-Wu Zheng & Mark Reid BeSSeL/NJU/CFA). The green ⊙ sign indicates the location of the Sun. The Galactic center is at the origin. Our candidates are designated by blue pluses (Pair-1) and red crosses(Pair-2).

円盤の縦方向

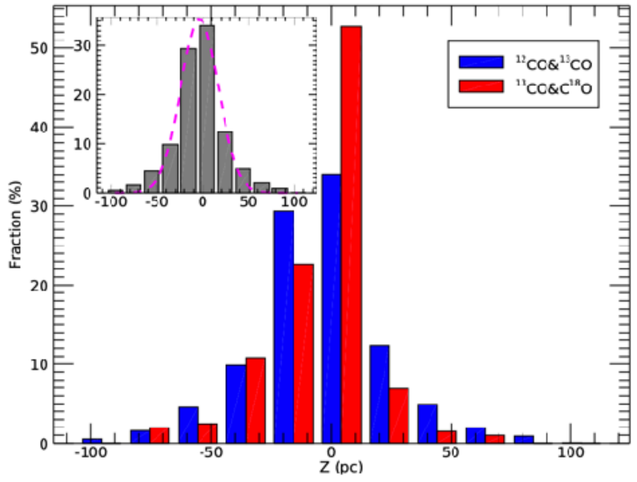

Fig. 8: The vertical distribution. The blue and red bars represents the Pair-1 and Pair-2 selected sources, respectively. The pink dashed curve in the inset is a Gaussian fit to the overall distribution with σ = 36 pc (FWHM = 85 pc).